Nanoscale

PAPER

View Article Online
View Journal

Cite this: DOI: 10.1039/d6nr00581k

Real-time visualization of plasmonic nanoparticle growth dynamics by high-speed atomic force microscopy

Fuma Wakabayashi, [a] Kenta Tamaki, [b] Feng-Yueh Chan, [b] Takayuki Uchihashi, [b,c] Prabhat Verma [a] and Takayuki Umakoshi *[a]

Plasmonic nanoparticles generate a strongly localized and enhanced light field through localized surface plasmon resonance, thereby playing a central role in plasmonics and nanophotonics. Because the optical properties of plasmonic nanoparticles are highly sensitive to their size and shape, nanoscale visualization of nanoparticle growth is crucial for detailed understanding of growth mechanisms and precise control of particle geometry. However, it is not possible to visualize the rapid growth dynamics using conventional imaging techniques. In this study, we demonstrate *in situ* real-time observation of silver nanoparticle (AgNP) growth dynamics at the single-particle level using high-speed atomic force microscopy (HS-AFM). We employed a photoreduction method, which enables reliable control of AgNP formation by laser irradiation. By integrating a stand-alone tip-scan HS-AFM with an optical setup for photoreduction, we successfully captured real-time movies showing the nucleation and subsequent growth of AgNPs at the single-particle level. Furthermore, quantitative single-particle analysis revealed particle-to-particle variations in growth dynamics. The growth dynamics were further studied at different laser intensities, revealing intensity-dependent growth rates and the balance between nucleation and growth. This study establishes HS-AFM as a novel microscopic platform for *in situ* visualization of plasmonic nanoparticle growth and will contribute to advances in plasmonics and materials science.

Received 10th February 2026,
Accepted 22nd May 2026

DOI: 10.1039/d6nr00581k

rsc.li/nanoscale

Introduction

Plasmonic nanoparticles, such as gold and silver nanoparticles, generate strongly localized and enhanced light field through localized surface plasmon resonance, and have therefore been widely employed in various plasmonic applications.[1–10] In general, plasmonic nanoparticles are chemically synthesized *via* the reduction of metal ions using reducing agents.[11–14] In such chemical synthesis, precise control of the size and shape of nanoparticles is crucial, as these factors strongly influence plasmonic properties such as the resonance wavelength and field enhancement factor.[1,10–12,15–18] Visualization of the growth process of plasmonic nanoparticles at the single-particle level is thus essential for a detailed understanding of their growth mechanisms and for achieving better control of the geometries of plasmonic nanoparticles. However, optical microscopy does not provide sufficient spatial resolution to precisely observe the size and shape of a single nanoparticle. In contrast, atomic force microscopy (AFM) offers nanoscale spatial resolution, enabling direct observation of individual nanoparticles. Nevertheless, its imaging speed is insufficient to track the growth process of nanoparticles. To observe the growth dynamics of individual plasmonic nanoparticles, both nanoscale spatial resolution and sufficient temporal resolution to follow the growth process are required.

In this study, we achieved *in situ* real-time observation of growth dynamics of silver nanoparticles (AgNPs) at the single-particle level using high-speed AFM (HS-AFM). HS-AFM is a powerful microscopic technique that simultaneously offers high spatial and temporal resolutions, providing a spatial resolution comparable to that of conventional AFM (~1 nm) and a typical temporal resolution of >10 frames per second (fps).[19] Owing to its great imaging capability, HS-AFM has made significant contributions to biological research by visualizing dynamic motions of functional proteins under physiological conditions.[20–26] In recent years, HS-AFM has also been applied to other research fields, including materials science and organic chemistry.[27–38] In particular, HS-AFM visualiza-

[a]*Department of Applied Physics, The University of Osaka, 2-1 Yamadaoka, Suita, Osaka 565-0871, Japan. E-mail: umakoshi@ap.eng.osaka-u.ac.jp*
[b]*Department of Physics, Nagoya University, Furo-cho, Chikusa-ku, Nagoya, Aichi 464-8602, Japan*
[c]*Exploratory Research Center on Life and Living Systems, National Institutes of Natural Sciences, 5-1 Higashiyama, Myodaiji, Okazaki, Aichi 444-8787, Japan*

tion of the nucleation and growth dynamics of supramolecular assemblies has been recently reported.[34,35] Therefore, plasmonic nanoparticle growth represents a suitable target for HS-AFM, which can provide unique insights into growth dynamics. To effectively observe the formation and growth of AgNPs, we employed photoreduction of silver ions.[39–42] In the photoreduction reaction, silver ions are reduced and grow into nanoparticles upon light irradiation. As we can easily switch on and off the reaction by light, the photoreduction method enables reliable control over nanoparticle growth and facilitates HS-AFM measurements. To effectively combine photoreduction with HS-AFM observation, we employed a tip-scan HS-AFM.[43,44] Unlike conventional HS-AFM, in which imaging is performed by scanning the sample stage, tip-scan HS-AFM rapidly scans the tip. Importantly, tip-scan HS-AFM is implemented as a stand-alone system so that it can be mounted on an inverted optical microscope, which greatly facilitates reliable integration with optical techniques.[32,45,46] Furthermore, evanescent light was introduced at the substrate surface *via* total internal reflection to induce the photoreduction reaction. Because the evanescent field is localized within a few hundred nanometers from the substrate surface, the formation and growth of AgNPs can be selectively induced only near the surface, resulting in stable and reliable HS-AFM operation. Using this developed system, we successfully captured real-time movies of the nucleation and subsequent growth of AgNPs at the single-nanoparticle level. Direct visualization of the growth process at the single-particle level provides new insights into plasmonic nanoparticle synthesis and represents a significant advance in the field of plasmonics.

Results & discussion

Experimental setup for HS-AFM observation of AgNP growth

Fig. 1 shows a schematic of the experimental setup for HS-AFM observation of the AgNP growth. A custom-built tip-scan HS-AFM system was installed on an inverted optical microscope. Details of the tip-scan HS-AFM system are described in previous studies.[32,43] We constructed a total internal reflection illumination setup beneath the tip-scan HS-AFM, which was similar to that used in objective-type total internal reflection fluorescence (TIRF) microscopy. A laser beam (Cobolt, Samba 0532-04-01-0100-700, λ = 532 nm) was expanded using a beam expander. It was then weakly focused at the pupil plane of an oil-immersion objective lens using a lens (f = 300 mm) such that a collimated laser beam emerged from the objective lens. By introducing the focused beam through the peripheral region of the objective, the laser beam was emitted from the objective with an angle larger than the critical angle. Consequently, the laser beam was totally internally reflected and only an evanescent light field was generated on the other side of the glass substrate, which was localized near the substrate surface. This configuration confined the photoreduction reaction to the vicinity of the substrate, while suppressing photoreduction in the bulk solution away from the substrate. This is important for stable HS-AFM operation, as the formation of a large number of AgNPs in the bulk solution can disturb HS-AFM measurements. To observe the photoreduction reaction and the formation of AgNPs, we adjusted the tip position to the center of the illumination spot. The illumination spot size was approximately 10 μm (corresponding to an area of ~80 μm^2). For photoreduction of AgNPs, we prepared an aqueous solution containing eosin-Y-disodium (eosin) (10 μM), *N*-methyldiethanolamine (MDEA) (1 mM), and $AgNO_3$ (0.5 mM). Eosin acted as a photosensitizer, while MDEA served as a reducing agent to reduce silver ion supplied from $AgNO_3$. The mechanism of the photoreduction reaction is described in previous studies.[41,42] The solution was dropped onto a piranha-cleaned glass substrate, and the photoreduction reaction was observed *in situ* using a tip-scan HS-AFM.

HS-AFM movies of AgNP growth dynamics

Using the constructed experimental system, we performed *in situ* HS-AFM video recording of the processes of nucleation and growth of AgNPs under photoreduction at an imaging rate of 1 fps with an image size of 300 × 300 nm^2. Laser irradiation was initiated at 0 s with a laser intensity of 10 W cm^{-2}, and the substrate surface was continuously illuminated thereafter. As shown in Fig. 2a and SI Movie S1, we successfully observed the nucleation of small AgNPs several seconds after the onset of laser irradiation. As a control measurement, we also performed

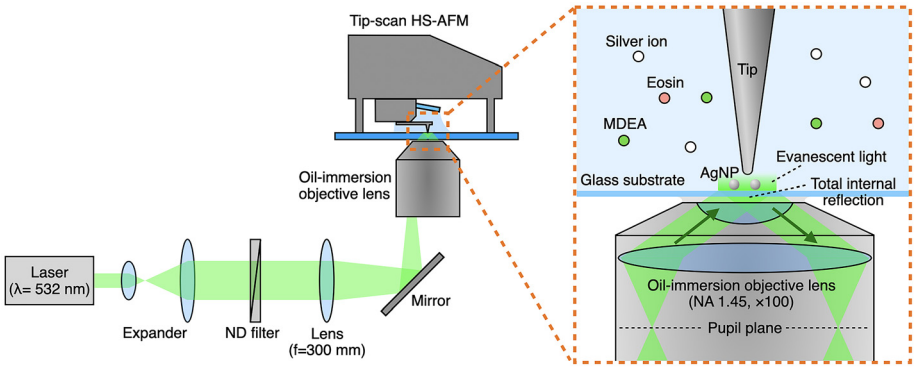

Fig. 1 Experimental setup for HS-AFM observation of the AgNP growth.

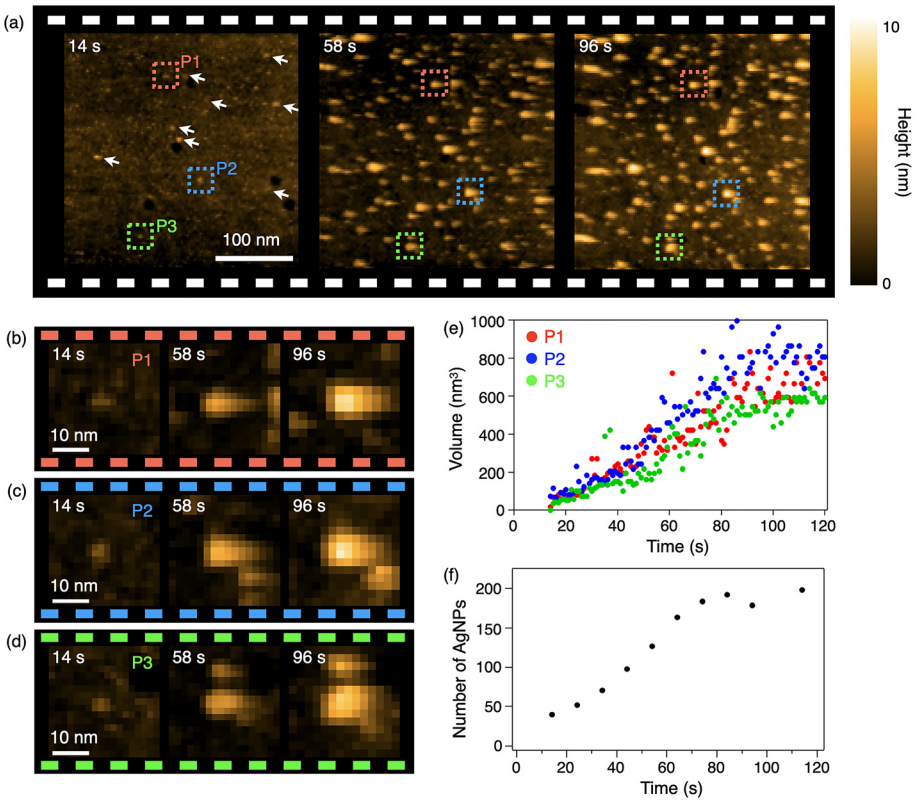

Fig. 2 (a) Clipped HS-AFM images showing the growth of AgNPs at a laser intensity of 10 W cm^{-2}. White arrows indicate the representative AgNPs generated by photoreduction. (b–d) Magnified HS-AFM images of AgNPs **P1**, **P2**, and **P3**, respectively, corresponding to the red, blue, and green dotted squares in (a). (e) Temporal evolution of the volume of the corresponding AgNP **P1**, **P2**, and **P3**. (f) Temporal evolution of the number of AgNPs within the HS-AFM field of view.

HS-AFM observations in the absence of the reducing agents ($AgNO_3$ only). As another control, we also observed outside the laser irradiation spot by HS-AFM. In both cases, particle formation was not observed, as shown in SI Movies S2 and S3, confirming that the observed objects in Fig. 2a were AgNPs generated through photoreduction. It should be noted that the small dark pits in the HS-AFM images are inherent features of the glass substrate and are unrelated to the AgNP formation. The number of AgNPs increased with time, indicating that nucleation proceeded continuously. In addition, the size of each AgNP increased over time due to particle growth. Fig. 2b–d represent magnified HS-AFM images to clearly show individual AgNPs, corresponding to **P1**, **P2**, and **P3** indicated by the dotted squares in Fig. 2a. The corresponding HS-AFM movies for **P1**, **P2**, and **P3** are also provided in SI Movies S4–S6, respectively. The growth of individual AgNPs was clearly visualized over time. Because HS-AFM provides precise height information, Fig. 2e presents the temporal evolution of the volumes of individual AgNPs in Fig. 2b–d. We assumed a hemispherical geometry immobilized on the substrate and estimated the volume from the measured heights as the hemispherical radius. The temporal evolution of the heights of the corresponding particles was also included in SI Fig. S1a. The volumes approximately linearly increased over the observation period. The growth rates of individual AgNPs were similar, with slight variations. Owing to the high spatiotemporal resolution of HS-AFM, the growth rate was quantitatively estimated to be approximately 7.2 nm^3 s^{-1}. These AgNPs eventually grew to a volumes of ~720 nm^3 after 120 s, corresponding to a height of 7.0 nm. Because nucleation occurred almost instantaneously within a single HS-AFM frame, the volume increase during nucleation could not be quantified accurately. Nevertheless, we found that it was at least on the order of several nm^3 s^{-1}. Furthermore, the number of AgNPs within the field of view of HS-AFM was counted, as shown in Fig. 2f. The particle number initially increased monotonically, and then interestingly, it was gradually saturated at approximately 200 particles at around 80 s. This behavior indicates that the nucleation and growth process occurred simultaneously when the particle density was low, and the growth process became dominant beyond a certain particle density because the particle growth is energetically more favorable than further nucleation. In addition, we confirmed that influence of tip scanning to AgNP formation was negligible. After AgNP formations, we stopped laser irradiation and observed the surrounding areas outside the originally scanned area, as shown in SI Fig. S2 and Movie S7. The particle sizes and distributions were almost the same inside and outside the tip-scanned area, indicating that tip scanning did not noticeably affect particle growth.

Next, we investigated the growth process of AgNPs at a higher laser intensity (60 W cm^{-2}), as shown in Fig. 3a and SI Movie S8. In this case, instability in HS-AFM operation and mechanical drift were observed for around 50 s immediately after the laser irradiation, probably due to the thermal drift caused by intense incident laser that perturbed the HS-AFM imaging conditions. In addition, optical radiation pressure from the incident laser may have contributed to this instability. Therefore, tracking of identical AgNPs was not possible before 50 s. Nevertheless, it was still possible to count the number of particles in the field of view before 50 s, and we could still observe that nucleation proceeded rapidly immediately after laser irradiation. After stabilization of the HS-AFM imaging, we further observed a gradual increase in the sizes of individual AgNPs, which is also clearly shown in Fig. 3b–d and SI Movies S9–S11. Single-particle analysis of the volume evolution is shown in Fig. 3e, where the volume was estimated from the height shown in SI Fig. S1b. It should be noted that this single-particle analysis was performed using data acquired after 50 s because of the initial mechanical drift mentioned above. The AgNPs exhibited a growth behavior similar to that observed at a laser intensity of 10 W cm^{-2} (Fig. 2e). However, individual AgNPs showed slightly different growth dynamics. The volume of AgNPs **P1** and **P2** increased with growth rates of approximately 8.8 nm^3 s^{-1}, whereas AgNP **P3** exhibited a faster growth rate of 15.2 nm^3 s^{-1}. Interestingly, at around 170 s, the growth rates of AgNP **P1** and **P3** increased to 33.2 and 29.2 nm^3 s^{-1}, respectively, while the growth rate of AgNP **P2** remained constant during the observation period. Such heterogeneous growth behavior between individual particles has also been observed through transmission electron microscopy (TEM) in previous reports.[47,48] Our HS-AFM observation supports the previous findings. Although the detailed mechanism underlying these differences is still under investigation, this behavior can be attributed to variations in the local environment surrounding each AgNP. For example, differences in the spatial distribution of neighboring AgNPs, the internal molecular packing order of each AgNP, and the local concentration of silver ions around individual particles can influence growth dynamics. In addition, nearby small silver nuclei may have merged to form a larger AgNP, thereby increasing the apparent growth rate. Local non-uniformity of the glass substrate surface may also affect growth dynamics. Owing to the powerful imaging capability of HS-AFM, such heterogeneous growth behavior of individual AgNPs was quantitatively visualized at the nanoscale. AgNPs **P1**, **P2** and **P3** eventually grew to volumes of approximately 2.36×10^3, 1.52×10^3, and 3.24×10^3 nm^3 after 235 s, corresponding to heights of 10.4, 9.0, and

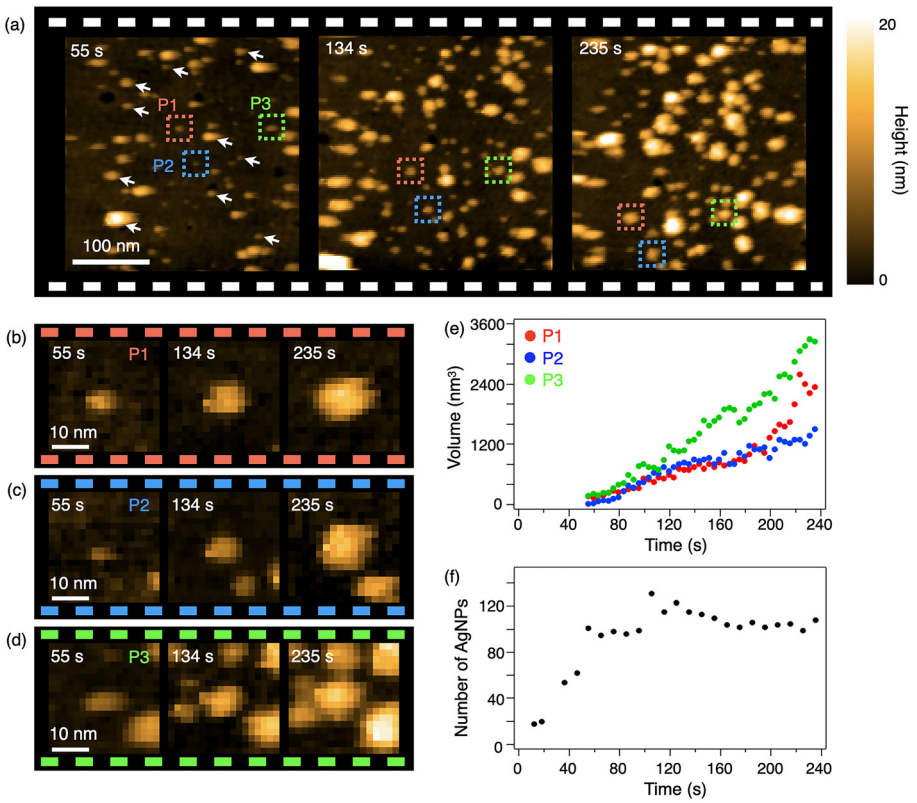

Fig. 3 (a) Clipped HS-AFM images showing the growth of AgNPs at a laser intensity of 60 W cm^{-2}. White arrows indicate the representative AgNPs generated by photoreduction. (b–d) Magnified HS-AFM images of AgNPs **P1**, **P2**, and **P3**, respectively, corresponding to the red, blue, and green dotted squares in (a). (e) Temporal evolution of the volume of the corresponding AgNP **P1**, **P2**, and **P3**. (f) Temporal evolution of the number of AgNPs within the HS-AFM field of view.

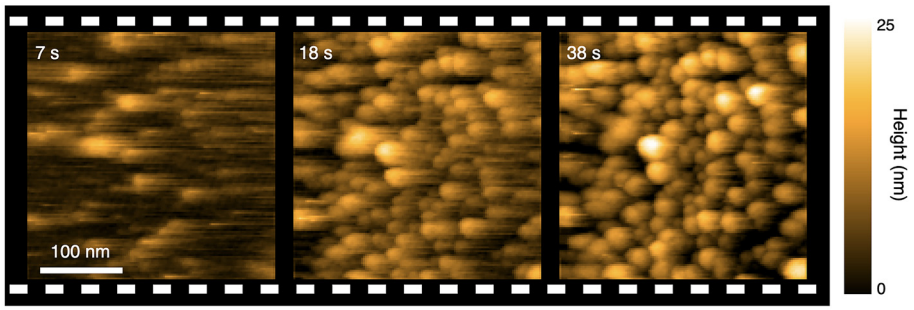

Fig. 4 Clipped HS-AFM images showing the growth of AgNPs at a laser intensity of 480 W cm^{-2}.

11.6 nm, respectively. We also counted the number of AgNPs within the HS-AFM field of view (Fig. 3f). Although the particle number first increased, it was almost saturated at 60 s, which was earlier than that observed at 10 W cm^{-2}. Moreover, the number of particles was eventually approximately 100, which was much fewer than that observed in the case of laser intensity of 10 W cm^{-2}. To the best of our knowledge, this inverse relationship between laser intensity and particle density has not been previously observed, which provides a novel insight into particle formation mechanisms. We attribute this behavior to faster particle growth at higher laser intensity, which reduces the local concentration of silver ions available for new nucleation events, thereby decreasing the probability of nucleation and resulting in a lower particle density.

Finally, we further increased the laser intensity to 480 W cm^{-2}. Under this condition, nucleation and growth of AgNPs occurred extremely rapidly, and the substrate surface was rapidly covered with abundant AgNPs within a few seconds, as shown in Fig. 4 and SI Movie S12. Therefore, statistical and quantitative analysis of the growth processes of individual particles was not feasible. Nevertheless, we observed a remarkably high growth rate and a very high density of AgNPs occupying the substrate surface at this high laser intensity.

Conclusion

In this study, we achieved *in situ* real-time visualization of the nucleation and growth of AgNPs at the single-particle level using HS-AFM. By integrating tip-scan HS-AFM with evanescent-field-induced photoreduction, we captured real-time movies of nanoparticle formation and subsequent growth with high spatiotemporal resolution. Quantitative analyses of individual particles revealed particle-to-particle variations in growth dynamics, highlighting the significant imaging capability of HS-AFM to directly probe growth processes.

Among various imaging techniques, liquid-cell TEM is another powerful tool for observing growth dynamics of metallic nanoparticles.[47,48] TEM typically provides higher spatial resolution than HS-AFM. Therefore, it is more effective for studying nucleation processes at the atomic scale. In contrast, HS-AFM provides height information in addition to lateral information, which is beneficial to study three-dimensional morphological dynamics. In addition, in many liquid-cell TEM studies, the electron beam is used not only for imaging but also for driving particle formation through beam-induced reduction of metal ions. In that sense, our HS-AFM system can independently control observation and particle formation, providing greater flexibility in exploring particle formation conditions. At present, HS-AFM measurements were performed under limited reaction conditions. Further studies under a variety of reaction conditions will contribute to elucidating the detailed growth mechanism of plasmonic nanoparticles. For example, we can extensively study the dependence of growth dynamics on the concentrations of silver ions, photosensitizer, and reducing agents. Moreover, by adding capping agents for shape control, observation of plasmonic nanostructures with different shapes, such as silver nanorods, would provide valuable insights. Extending this approach to other plasmonic materials, such as gold and aluminum, will also deepen our understanding of plasmonic nanoparticle growth. Overall, HS-AFM enables direct nanoscale visualization of plasmonic nanoparticle growth, establishing a promising microscopic platform for elucidating growth mechanisms and advancing plasmonics and materials science.

Conflicts of interest

The authors have no conflicts of interest to declare.

Data availability

The data supporting this article have been included as part of the supplementary information (SI). Supplementary information: temporal evolution of AgNP heights, HS-AFM image of tip-scanned area and non-scanned area and all HS-AFM movies of AgNP nucleation and growth. See DOI: https://doi.org/10.1039/d6nr00581k.

Acknowledgements

This work was partially supported by JST FOREST (JPMJFR233Z), JSPS Grant-in-Aid for Scientific Research

(KAKENHI) (Grant in Aid for Scientific Research (B) JP24K01385, Grant-in-Aid for Transformative Research Areas (A) Publicly Offered Research "Chiral materials science pioneered by the helicity of light" JP25H01624, Grant-in-Aid for Transformative Research Areas (A) Publicly Offered Research "Materials science of meso-hierarchy" JP24H01717, Grant-in-Aid for Challenging Research (Exploratory) JP24K21718), and a research grant from the Takahashi Industrial and Economic Research Foundation.

References

1 S. A. Maier and H. A. Atwater, *J. Appl. Phys.*, 2005, **98**, 011101.
2 M. Moskovits, *J. Raman Spectrosc.*, 2005, **36**, 485–496.
3 K. A. Willets and R. P. V. Duyne, *Annu. Rev. Phys. Chem.*, 2007, **58**, 267–297.
4 J. N. Anker, W. P. Hall, O. Lyandres, N. C. Shah, J. Zhao and R. P. Van Duyne, *Nat. Mater.*, 2008, **7**, 442–453.
5 S. Kawata, Y. Inouye and P. Verma, *Nat. Photonics*, 2009, **3**, 388–394.
6 M. L. Brongersma, N. J. Halas and P. Nordlander, *Nat. Nanotechnol.*, 2015, **10**, 25–34.
7 S. Linic, U. Aslam, C. Boerigter and M. Morabito, *Nat. Mater.*, 2015, **14**, 567–576.
8 B. Ranjan, Y. Saito and P. Verma, *Appl. Phys. Express*, 2016, **9**, 032401.
9 J. J. Baumberg, J. Aizpurua, M. H. Mikkelsen and D. R. Smith, *Nat. Mater.*, 2019, **18**, 668–678.
10 Y. Hang, A. Wang and N. Wu, *Chem. Soc. Rev.*, 2024, **53**, 2932–2971.
11 L. Scarabelli, A. Sánchez-Iglesias, J. Pérez-Juste and L. M. Liz-Marzán, *J. Phys. Chem. Lett.*, 2015, **6**, 4270–4279.
12 V. Pawlik, S. Zhou, S. Zhou, D. Qin and Y. Xia, *Chem. Mater.*, 2023, **35**, 3427–3449.
13 I. Jung, S. Lee, S. Lee, J. Kim, S. Kwon, H. Kim and S. Park, *Chem. Rev.*, 2025, **125**, 7321–7388.
14 A. Sati, T. N. Ranade, S. N. Mali, H. K. A. Yasin and A. Pratap, *ACS Omega*, 2025, **10**, 7549–7582.
15 K. L. Kelly, E. Coronado, L. L. Zhao and G. C. Schatz, *J. Phys. Chem. B*, 2003, **107**, 668–677.
16 A. Callegari, D. Tonti and M. Chergui, *Nano Lett.*, 2003, **3**, 1565–1568.
17 T. K. Sau and C. J. Murphy, *J. Am. Chem. Soc.*, 2004, **126**, 8648–8649.
18 R. Kato, T. Umakoshi and P. Verma, *J. Phys. Chem. C*, 2021, **125**, 20397–20404.
19 T. Ando, N. Kodera, E. Takai, D. Maruyama, K. Saito and A. Toda, *Proc. Natl. Acad. Sci. U. S. A.*, 2001, **98**, 12468–12472.
20 N. Kodera, D. Yamamoto, R. Ishikawa and T. Ando, *Nature*, 2010, **468**, 72–76.
21 M. Shibata, H. Yamashita, T. Uchihashi, H. Kandori and T. Ando, *Nat. Nanotechnol.*, 2010, **5**, 208–212.
22 T. Uchihashi, R. Iino, T. Ando and H. Noji, *Science*, 2011, **333**, 755–758.
23 I. Casuso, J. Khao, M. Chami, P. Paul-Gilloteaux, M. Husain, J.-P. Duneau, H. Stahlberg, J. N. Sturgis and S. Scheuring, *Nat. Nanotechnol.*, 2012, **7**, 525–529.
24 T. Uchihashi, Y. Watanabe, Y. Nakazaki, T. Yamasaki, H. Watanabe, T. Maruno, K. Ishii, S. Uchiyama, C. Song, K. Murata, R. Iino and T. Ando, *Nat. Commun.*, 2018, **9**, 2147.
25 S. Nishiguchi, T. Furuta and T. Uchihashi, *Proc. Natl. Acad. Sci. U. S. A.*, 2022, **119**, e2208067119.
26 Y. Kanaoka, T. Mori, W. Nagaike, S. Itaya, Y. Nonaka, H. Kohga, T. Haruyama, Y. Sugano, R. Miyazaki, M. Ichikawa, T. Uchihashi and T. Tsukazaki, *Nat. Commun.*, 2025, **16**, 225.
27 T. Umakoshi, H. Udaka, T. Uchihashi, T. Ando, M. Suzuki and T. Fukuda, *Colloids Surf., B*, 2018, **167**, 267–274.
28 T. Fukui, T. Uchihashi, N. Sasaki, H. Watanabe, M. Takeuchi and K. Sugiyasu, *Angew. Chem., Int. Ed.*, 2018, **57**, 15465–15470.
29 Y. Nishizawa, S. Matsui, K. Urayama, T. Kureha, M. Shibayama, T. Uchihashi and D. Suzuki, *Angew. Chem., Int. Ed.*, 2019, **58**, 8809–8813.
30 N. Sasaki, J. Kikkawa, Y. Ishii, T. Uchihashi, H. Imamura, M. Takeuchi and K. Sugiyasu, *Nat. Chem.*, 2023, **15**, 922–929.
31 K. Tamaki, S. Datta, H. Hanayama, C. Ganser, T. Uchihashi and S. Yagai, *J. Am. Chem. Soc.*, 2024, **146**, 22166–22171.
32 K. Yang, F.-Y. Chan, H. Watanabe, S. Yoshioka, Y. Inouye, T. Uchihashi, H. Ishitobi, P. Verma and T. Umakoshi, *Nano Lett.*, 2024, **24**, 2805–2811.
33 C. van Ewijk, F. Xu, S. Maity, J. Sheng, M. C. A. Stuart, B. L. Feringa and W. H. Roos, *Angew. Chem., Int. Ed.*, 2024, **63**, e202319387.
34 K. Tamaki, H. Hanayama, S. Datta, F. Silly, Y. Wada, D. Hashizume, K. Adachi, T. Uchihashi, M. Kawano, C. Ganser and S. Yagai, *Chem*, 2026, **12**, 102818.
35 S. Kimura, K. Adachi, Y. Ishii, T. Komiyama, T. Saito, N. Nakayama, M. Yokoya, H. Takaya, S. Yagai, S. Kawai, T. Uchihashi and M. Yamanaka, *Nat. Commun.*, 2025, **16**, 3758.
36 Y. Nodera, Y. Watanabe, Y. Ishii, G. Watanabe, C. Ganser, T. Uchihashi and K. Sugiyasu, *Angew. Chem., Int. Ed.*, 2025, **64**, e202512811.
37 Y. C. Cheng, R. Ohashi, N. Kotani, I. Hida, T. Naganuma, M. Ueda and H. Matsushima, *Electrochim. Acta*, 2025, **543**, 147564.
38 H. Matsui, C. Ganser, K. Tamaki, Q. Liu, F.-Y. Chan, T. Uchihashi, P. Verma, Y. Sagara, S. Yagai and T. Umakoshi, *Langmuir*, 2026, **42**, 448–454.
39 H. Hada, Y. Yonezawa, A. Yoshida and A. Kurakake, *J. Phys. Chem.*, 1976, **80**, 2728–2731.
40 M. Sakamoto, M. Fujistuka and T. Majima, *J. Photochem. Photobiol., C*, 2009, **10**, 33–56.
41 L. Balan, J.-P. Malval, R. Schneider, D. Le Nouen and D.-J. Lougnot, *Polymer*, 2010, **51**, 1363–1369.
42 T. Umakoshi, T. Yano, Y. Saito and P. Verma, *Appl. Phys. Express*, 2012, **5**, 052001.

43 S. Fukuda, T. Uchihashi, R. Iino, Y. Okazaki, M. Yoshida, K. Igarashi and T. Ando, *Rev. Sci. Instrum.*, 2013, **84**, 073706.
44 Y. Suzuki, N. Sakai, A. Yoshida, Y. Uekusa, A. Yagi, Y. Imaoka, S. Ito, K. Karaki and K. Takeyasu, *Sci. Rep.*, 2013, **3**, 2131.
45 T. Umakoshi, S. Fukuda, R. Iino, T. Uchihashi and T. Ando, *Biochim. Biophys. Acta, Gen. Subj.*, 2020, **1864**, 129325.
46 C. Ganser, S. Nishiguchi, F.-Y. Chan and T. Uchihashi, *Sci. Adv.*, 2025, **11**, eads3010.
47 T. J. Woehl, J. E. Evans, I. Arslan, W. D. Ristenpart and N. D. Browning, *ACS Nano*, 2012, **6**, 8599–8610.
48 X. Wang, S. Xue, X. Qi, D. Song, L. Liu, Y. Zhao, P. Chen, M. L. Sushko, K. M. Rosso and X. Zhang, *Chem. Mater.*, 2025, **37**, 2569–2580.